

Optimization of Information Reconciliation for Decoy-State Quantum Key Distribution over a Satellite Downlink Channel

Thomas Scarinzi, Davide Orsucci, Marco Ferrari, *Member, IEEE*, and Luca Barletta, *Member, IEEE*

Abstract—Quantum Key Distribution (QKD) is a cryptographic solution that leverages the properties of quantum mechanics to be resistant and secure even against an attacker with unlimited computational power. Satellite-based links are important in QKD because they can reach distances that the best fiber systems cannot. However, links between satellites in Low Earth Orbit (LEO) and ground stations have a duration of only a few minutes, resulting in the generation of a small amount of secure keys. In this context, we investigate the optimization of the information reconciliation step of the QKD post-processing in order to generate as much secure key as possible. As a first step, we build an accurate model of the downlink signal and Quantum Bit Error Rate (QBER) during a complete satellite pass, which are time-varying due to three effects: (i) the varying link geometry over time, (ii) the scintillation effect, and (iii) the different signal intensities adopted in the Decoy-State protocol. Leveraging the a-priori information on the instantaneous QBER, we improve the efficiency of Information Reconciliation (IR) (i.e., the error correction phase) in the Decoy-State BB84 protocol, resulting in a secure key that is almost 3% longer for realistic scenarios.

Index Terms—Quantum Key Distribution, Quantum Cryptography, Decoy-State Method, BB84, Information Reconciliation, Low-Density Parity Check Codes, Satellite Free-Space Optical Communications, Scintillation.

I. INTRODUCTION

THE future advent of quantum computers represents an existential security threat for the cryptographic systems that are used nowadays. When Peter Shor invented the quantum algorithm capable of factoring numbers with polynomial complexity [1], it basically rendered Rivest-Shamir-Adleman (RSA) insecure against an adversary having access to a quantum computer. Additionally, the period finding primitive present in Shor's algorithm allows an attacker to break also Elliptic Curve Cryptosystems (ECC) [2]. Furthermore, the problem is already pressing today because of the so called “harvest now, decrypt later” attack, in which the adversaries could store the communications now and decrypt them in the future when they will have the sufficient computational power.

T. Scarinzi was with Politecnico di Milano, 20133 Milan, Italy (email: thomasscarinzi@gmail.com)

D. Orsucci is with the Institute of Communications and Navigation, Deutsches Zentrum für Luft- und Raumfahrt (DLR), 82234 Weßling, Germany (email: davide.orsucci@dlr.de).

M. Ferrari is with the Consiglio Nazionale delle Ricerche, Istituto di Elettronica e di Ingegneria dell'Informazione e delle Telecomunicazioni, Italy (email: marcopietro.ferrari@cnr.it)

L. Barletta is with the Dipartimento di Elettronica, Informazione e Bioingegneria, Politecnico di Milano, 20133 Milan, Italy (email: luca.barletta@polimi.it)

To address this problem, one of the possible solutions is QKD, which allows to securely exchange two identical keys (or passwords) between two users. These keys may later be used to secure the communication between the two users through a symmetric cryptosystem.

The development of QKD technology for ground-based systems has reached a rather high level of maturity and is already commercially available as a certified product [3]. A major hurdle is that when a quantum state propagates through an optical fiber, both photon loss (attenuation) and decoherence processes cause its fidelity to decay exponentially with distance, setting a hard limit on the maximum distance in which ground-based QKD is feasible. Sat-QKD constitutes a promising solution to this problem, introducing satellites into the game in order to connect distant users. Indeed, in free-space channels, transmission generally decays quadratically with distance due to beam divergence, with additional losses arising due to atmospheric absorption and receiver terminal finite optical transmission. This quadratic scaling enables establishing QKD links over long distances, sufficient to connect an Optical Ground Station (OGS) and a satellite in LEO with optical terminals of relatively small size. The advantage of Sat-QKD, with respect to fiber-based systems, is that to achieve these long distance communications, only one satellite is needed as a trusted node, provided that during its orbit it can establish connections with all the users [4]. Instead, to reach these distances with ground-based systems, many relays are needed and therefore many trusted nodes on the ground, which pose more vulnerability issues compared to a single satellite in LEO.

Sat-QKD faces several challenges, such as weather dependence, link availability, hardware and deployment complexity, and costs. Anyway, in recent years there has been significant progress, with several missions demonstrating feasibility and operational capabilities. The Chinese satellite *Micius* pioneered long-distance QKD with successful Decoy-State BB84 key exchange over distances exceeding 1,200 km [5], together with the first QKD encrypted video call between Vienna and Beijing in 2017 [6]. Following this, the Jinan-1 satellite extended QKD applications in urban-scale networks and emphasized integration with terrestrial fiber infrastructures [7], while Tiangong-2 demonstrated QKD with small-sized payload. In Europe, missions such as *SAGA* and *Eagle-1* are designed to deploy Prepare and Measure (PM) QKD payloads in LEO, aiming for operational secure links between ground stations [8], [9]. More recently, CubeSat missions such

as *QUBE*, developed by the Deutsches Zentrum für Luft- und Raumfahrt (DLR), and its successor *QUBE-II*, aim to validate miniaturized quantum payloads and investigate their performance in constrained orbital environments [10], [11]. These efforts collectively indicate a shift from experimental demonstrations to the early stages of operational satellite QKD constellations. In this work, the objective is to optimize one of the most commonly used protocols, that is the Decoy-State BB84, in the context of Sat-QKD, by using the instant-by-instant channel model, instead of using the average loss during the downlink communication. The main factors in play are the transmission change due to the changing link distance and the turbulence-induced scintillation.

Paper novelty: The main contribution of this work is the optimization of the IR phase for Decoy-State BB84 under non-constant error rates. Such conditions arise in satellite-to-ground QKD downlinks due to channel dynamics, where the use of multiple pulse intensities in the Decoy-State protocol induces a signal-dependent QBER. In practice, the QBER can be accurately estimated by monitoring channel transmission with optical support equipment already required for beaconing and classical communication, as well as by measuring the error rate in the non-key-generating basis. Exploiting this a-priori information enables more efficient error correction during the IR stage of QKD post-processing, thereby extending the secure key length without hardware modifications and with only minor changes to the post-processing.

Paper organization: The remainder of this paper is organized as follows. Sec. II introduces the background on Information Reconciliation and QKD. Sec. III covers the link budget and Sec. IV the power scintillation, which combined give the downlink channel model. Sec. V present the model of the QBER in the QKD receiver. In Sec. VI we present details on the simulation implementation, whose result are presented in Sec. VII, evaluating the performance of adaptive Low-Density Parity-Check (LDPC)-based IR schemes under realistic channel conditions. Finally, Sec. VIII concludes the paper and discusses directions for future work.

II. PRELIMINARIES

This section provides the necessary background to understand the design and optimization of IR for Sat-QKD.

A. Information Reconciliation with LDPC Codes

Consider the case where Alice and Bob have two unequal but correlated bit strings, \mathbf{z}_A , \mathbf{z}_B , obtained by *sifting* a larger sequence of prepared and measured states. In direct Information Reconciliation Bob tries to retrieve the value \mathbf{z}_A while exchanging as little information as possible, similarly to what is done in error correction. The Cascade protocol [12] and LDPC-based schemes are among the most widely adopted approaches for IR. Here we focus on the latter, which were shown to have good performance for IR in QKD scenarios [13].

Let H be the parity check matrix of a (fixed) LDPC code. Alice computes the syndrome vector $\mathbf{s}_A = H \cdot \mathbf{z}_A \pmod{2}$ and

sends the message to Bob over a public channel. Bob locally computes $\mathbf{s}_B = H \cdot \mathbf{z}_B \pmod{2}$ and together with \mathbf{s}_A he gets

$$\mathbf{s} = \mathbf{s}_A + \mathbf{s}_B = H \cdot (\mathbf{z}_A + \mathbf{z}_B) = H \cdot \mathbf{e} \quad (1)$$

which means that \mathbf{s} is the syndrome associated with the error vector \mathbf{e} . If the syndrome \mathbf{s} has sufficient information on \mathbf{e} , a decoder can succeed in recovering its value.

In this work we consider IR based on Rateless Protograph LDPC codes. The protograph is a small bipartite graph that is used to generate the Tanner graph of the LDPC code by replicating the protograph multiple times and then connecting the copies by applying some circular shifts [14]. The main advantage of protograph codes for IR is that a single protograph can be used to generate LDPC codes of different block lengths by varying the lift factor (i.e. the number of replications of the protograph), thereby providing flexibility for different message lengths without requiring the design of a new code in each case. Besides, the convergence properties of BP decoding can be accurately predicted based on the protograph structure. In a rateless implementation, a sequence of parity-check matrices with decreasing code rates is defined a priori. For each reconciliation attempt, the most suitable code is selected, prioritizing the one with the lowest inefficiency; if decoding fails, the code rate is progressively lowered until convergence is achieved. In IR, the empirical inefficiency factor f quantifies the multiplicative overhead in information leakage relative to the asymptotically achievable limit. It is defined as

$$f = \frac{1 - R}{h_2(\phi)}, \quad (2)$$

where ϕ the error rate and R is the code rate at which convergence is reached, given by

$$R = \frac{n - m}{n} \quad (3)$$

with m the length of the syndrome \mathbf{s} and n the length of the sifted key. The IR rate is a critical parameter in QKD, as it directly impacts the final Secret Key Length (SKL): for every information bit revealed over the public channel, Alice and Bob must remove one bit from the corrected key to eliminate any knowledge potentially gained by Eve.

With rateless codes, the rate is automatically adapted to the channel reliability, without requiring an accurate a priori estimate of the error rate, thereby reducing inefficiency. Notably, this procedure converges within only a few iterations (almost always fewer than three), whereas Cascade typically requires hundreds of iterations [12]. This difference is especially critical in Sat-QKD, where the long link distance leads to round-trip times of on the order of tens of milliseconds.

B. Fundamentals of Quantum Key Distribution

QKD is the branch of quantum cryptography devoted to the distribution of secure keys between two endpoints with information-theoretic security, thereby providing a fundamental solution to the vulnerability introduced by Shor's algorithm. In this work, we focus on BB84, the earliest and simplest QKD protocol, proposed by Bennett and Brassard in 1984 [15].

For concreteness, we consider qubits encoded in the polarization degree of freedom. Conventionally, the Z -basis vectors are associated with the linear polarization states $|H\rangle = |0\rangle$ and $|V\rangle = |1\rangle$, where H and V denote horizontal and vertical polarization, respectively. The X -basis vectors correspond to diagonal ($|D\rangle = |+\rangle$) and anti-diagonal ($|A\rangle = |-\rangle$) polarizations. Since both bases are dichotomic, each can encode a single bit of information. After the quantum transmission, Alice and Bob discard all outcomes where they used different bases (e.g., Alice used X while Bob used Z). This step, called *sifting*, yields the *sifted key*. Typically, one basis (e.g., Z) is used for key generation, while the other (e.g., X) is reserved for parameter estimation.

To optimize protocol performance, it is beneficial to increase the probability p_Z of selecting the key-generation basis (Z basis). The probability that both Alice and Bob choose this basis is then p_Z^2 , while the probability that both choose the parameter-estimation basis (X basis) is $(1-p_Z)^2$. Hence, basis-selection probabilities become an optimization parameter of the protocol, whereas in the original BB84 formulation the Z and X bases were chosen with equal probability.

In essence, the security of BB84 relies on Eve's lack of knowledge about Alice's encoding basis. If she measures qubits in randomly chosen bases, she inevitably introduces errors, which increase the QBER.

The original BB84 protocol assumes perfect single-photon sources, which remain experimentally challenging. Instead, we consider an implementation using attenuated laser pulses, such that the mean photon number per pulse is less than one [16]. These Weak Coherent Pulses (WCP) introduce a vulnerability to Photon Number Splitting (PNS) attacks: whenever multiple photons are emitted, Eve could store one in a quantum memory and measure it later in the correct basis, without introducing detectable errors. A countermeasure, proposed in [17], is the use of *decoy states*. In this approach, Alice randomly modulates each pulse among two or more mean intensity levels. After Bob's detection stage, Alice reveals the chosen intensities, enabling a statistical test that guarantees a lower bound on the number of single-photon events received by Bob. On this subset of events, the standard BB84 security proof applies.

Using the Decoy-State method, Alice and Bob employ the observed measurement outcomes to derive lower bounds on the number of vacuum events ($s_{Z,0}^-$) and single-photon events ($s_{Z,1}^-$) in the Z basis, as well as an upper bound on the virtual QBER in the X basis for single-photon events that were actually measured in the Z basis ($\phi_{X,1}^+$). These bounds are then used to estimate the length ℓ of the extractable secret key [18], [19]

$$\ell = s_{Z,0}^- + s_{Z,1}^- (1 - h(\phi_{X,1}^+)) - \lambda_{\text{IR}} - \log_2 \frac{2}{\varepsilon_{\text{cor}}} - 6 \log_2 \frac{21}{\varepsilon_{\text{sec}}} \quad (4)$$

where λ_{IR} is the information leaked during IR, while ε_{cor} and ε_{sec} are the correctness and security parameters of the protocol, respectively. Specifically, ε_{cor} is the maximum probability that Alice's and Bob's keys differ, and ε_{sec} is the maximum

probability that any information about the key is available to Eve. In this work, we set $\varepsilon_{\text{cor}} = 10^{-15}$ and $\varepsilon_{\text{sec}} = 10^{-9}$.

C. Average vs Instantaneous Quantum Bit Error Rate

The empirical average QBER is defined as the ratio between the total number of errors and the total number of established bits.

$$\phi_X \equiv \text{QBER}_X := \frac{|\mathbf{x}_A \oplus \mathbf{x}_B|}{\text{len}(\mathbf{x}_A)}, \quad (5)$$

$$\phi_Z \equiv \text{QBER}_Z := \frac{|\mathbf{z}_A \oplus \mathbf{z}_B|}{\text{len}(\mathbf{z}_A)}, \quad (6)$$

where \mathbf{x}_A and \mathbf{x}_B (respectively, \mathbf{z}_A and \mathbf{z}_B) denote the binary vectors representing the sifted bits of Alice and Bob in the X (resp. Z) basis. Here, $|\mathbf{x}|$ indicates the Hamming weight of \mathbf{x} (i.e., the number of non-zero elements).

In [20], it was shown that the asymptotic key rate of a QKD protocol can be expressed as

$$R = 1 - h_2(\phi_X) - h_2(\phi_Z), \quad (7)$$

where $h_2(x) := -x \log_2(x) - (1-x) \log_2(1-x)$ is the binary entropy function. In this expression, $h_2(\phi_X)$ represents an upper bound on the information available to Eve, while $h_2(\phi_Z)$ denotes the asymptotic lower bound on the information required for information reconciliation. In particular, when $\text{QBER}_X = \text{QBER}_Z = \phi$, the threshold QBER above which the key rate vanishes is obtained by solving

$$1 - 2h_2(\phi) \geq 0, \quad (8)$$

which yields $\phi \lesssim 11\%$.

When the channel is time-varying, each qubit (or each WCP) can experience a different error probability. This is the case in Free Space Optical (FSO) satellite channels, where Alice and Bob may estimate the instantaneous error probability. For instance, classical optical support systems (e.g., classical communication or beacon signals) can be used to infer the probability that a single photon transmitted by Alice through the quantum channel is detected by Bob, since classical and quantum channels exhibit proportional transmission. This enables instantaneous error-rate estimation: for example, if detector dark counts and background light dominate and remain constant (or vary slowly), the error rate increases whenever the quantum channel transmission decreases.

This a priori reliability information can be exploited to improve the efficiency of IR. One possible strategy is to group bits into blocks with approximately equal error probability ϕ_j , and to perform IR independently on each block. Asymptotically, the average information required for IR is

$$\lambda_{\text{IR}} \approx \sum_j n_j h_2(\phi_j) \leq nh_2(\langle \phi \rangle), \quad (9)$$

where n_j is the number of bits with error probability ϕ_j , and $\langle \phi \rangle = \frac{1}{n} \sum_j n_j \phi_j$ is the average QBER. The inequality follows from the concavity of the binary entropy. This approach allows extraction of a longer secure key. However, due to finite-size effects, this advantage emerges only for very large block sizes.

A more practical strategy is to apply IR to large blocks of bits with different reliabilities, while providing the reliability

estimates to the LDPC decoder in the form of Log-Likelihood Ratio (LLR)s. An efficient decoder can then exploit this side information to approach the asymptotic rate.

The objective of the present work is to exploit such a priori reliability information to improve the efficiency of IR in Decoy-State BB84. This reduces the information leakage, λ_{IR} , thereby increasing the secret key length according to (4). Note, however, that the estimation of the virtual X -basis QBER for single-photon events, $\phi_{X,1}$, must still be performed using the average QBER, as in the standard block-wise Decoy-State analysis.

III. LINK BUDGET MODEL

In this work, the considered communication channel is a FSO downlink from a LEO satellite to an OGS. Specifically, we consider a Sun-synchronous orbit, which guarantees that there are nighttime passes every day throughout the year. We fix a link reference scenario which reproduces the KIODO measurement campaign carried out by DLR [21]. The satellite is in a circular Sun-synchronous orbit at altitude $h_{\text{sat}} = 567$ km above the Earth (using as mean radius $R_E = 6371$ km) and consider a pass where the satellite reaches a maximum elevation of 80° , while the link is established above a minimum elevation of 20° . For the receiver we employ the physical parameters of the OGS at the DLR Institute of Communications and Navigation (OGS-KN). A summary of the parameters employed in the simulations are reported in Table I, which are realistic for near-term Sat-QKD implementations.

In our context, the link budget is a model of the end-to-end efficiency for the FSO channel. The factor that we take into account in the end-to-end loss are

$$\eta = \eta_{\text{coll}} \cdot \eta_{\text{pointing}} \cdot \eta_{\text{atm}} \cdot \eta_{\text{Rx}} \cdot \eta_{\text{det}} \cdot \eta_{\text{scint}} \quad (10)$$

which denote the collection efficiency, pointing loss, atmospheric loss, receiver internal loss, detector efficiency and the (stochastic) scintillation effect. Since these factors enter multiplicatively in the link budget, they are usually expressed in dB units and, for convenience, we introduce the function

$$\text{dB}[x] := 10 \log_{10}(x). \quad (11)$$

a) *Collection efficiency*: The most prominent factor in the link budget is the receiver collection efficiency η . For communications between terminals that are in the far field from each other that is (approximately) given by the Friis equation [22]:

$$\eta_{\text{coll}} = G_{\text{Tx}} \cdot G_{\text{Rx}} \cdot L_{\text{free space}} \quad (12)$$

where G_{Tx} (G_{Rx}) is the transmitter (receiver) ideal antenna gain, $L_{\text{free space}} = \left(\frac{\lambda}{4\pi L}\right)^2$ is the free space loss, L is the link distance and λ is the wavelength. We assume $\lambda = 1550$ nm, as optical communication technology is most developed for the C-band. Upper bounds to the antenna gains are given by $G_{\text{Tx}} \leq \frac{4\pi A_{\text{Tx}}}{\lambda^2}$ ($G_{\text{Rx}} \leq \frac{4\pi A_{\text{Rx}}}{\lambda^2}$), where A_{Tx} (A_{Rx}) is the transmitter (receiver) antenna aperture area. The interpretation of Eq. (12) is that only a small fraction of the sent signal power is received because the beam spot at the OGS is much larger than the diameter of the telescope. Notice that η decreases quadratically

Name	Value	Unit	Description
<i>Global System Parameters</i>			
λ	1550	nm	Wavelength of the quantum signal
R_{Tx}	1	GHz	Transmitter pulse repetition rate
h_{sat}	567	km	Satellite orbital altitude
θ_{div}	5	μrad	Beam half-divergence angle
T_{pass}	330	s	Satellite pass duration
θ_{min}	20	deg	Minimum elevation angle
θ_{max}	80	deg	Maximum elevation angle
h_{OGS}	602	m	Altitude of the Optical Ground Station
D_{OGS}	0.8	m	OGS primary mirror diameter
$D_{\text{OGS}}^{\text{int}}$	0.3	m	OGS secondary mirror (obscuration) diameter
<i>Link Budget Parameters</i>			
η_{coll}	[sim.]	dB	Receiver collection efficiency
η_{atm}	[sim.]	dB	Loss from atmospheric absorption
η_{scint}	[sim.]	dB	Scintillation due to atmospheric turbulence
η_{pointing}	-3.0	dB	Loss due to pointing inaccuracies
η_{Rx}	-1.5	dB	Internal loss from receiver optics
η_{det}	-7	dB	Detector efficiency (equivalent to 20%)
<i>Scintillation Simulation Parameters</i>			
R_{sample}	40	kHz	Sampling frequency for scintillation simulation
$\tau_{\text{corr}}^{\text{max}}$	0.03	s	Time length of the simulation filter
Δ	1	s	Time between simulation filter updates
<i>QKD Protocol Parameters</i>			
p_Z	0.85	-	Probability of choosing the key generation basis
μ	0.59	-	Mean photon number of the signal state
ν	0.21	-	Mean photon number of the decoy state
p_{μ}	0.80	-	Probability of sending the signal state μ
p_{ν}	0.14	-	Probability of sending the decoy state ν
δ_{mis}	5	deg	Misalignment between Alice and Bob's bases
R_{noise}	3	kHz	Effective noise photon rate
t_{holdoff}	100	ns	Detector hold-off (dead) time
ε_{cor}	10^{-15}	-	Correctness parameter of the QKD protocol
ε_{sec}	10^{-9}	-	Security parameter of the QKD protocol

TABLE I: Reference parameters for the simulations.

with the distance L . The transmitted signal is modeled as a Gaussian beam with half-divergence θ_{div} . This is connected to the size of the transmitter aperture, D_{Tx} , which dictates the minimum beam divergence allowed by diffraction ($\theta_{\text{div}} \gtrsim \lambda/D_{\text{Tx}}$). Furthermore, we assume that the receiver telescope is a Cassegrain-type telescope, having a secondary circular mirror of diameter $D_{\text{OGS}}^{\text{int}}$ obscuring the primary one, having diameter D_{OGS} . The gains are thus computed as

$$G_{\text{Tx}} = \frac{8}{\theta_{\text{div}}^2} \quad \text{and} \quad G_{\text{Rx}} = \frac{\pi^2}{\lambda^2} (D_{\text{OGS}}^2 - (D_{\text{OGS}}^{\text{int}})^2). \quad (13)$$

In our model we use $\theta_{\text{div}} = 5$ μrad (half-divergence to $1/e^2$ intensity angle), which is achievable with current technology [5] and reasonably sized aperture on the satellite terminal ($D_{\text{Tx}} \approx 200$ mm). For the ground telescope we employ the values $D_{\text{OGS}} = 800$ mm and $D_{\text{OGS}}^{\text{int}} = 300$ mm, which are the physical dimensions of the OGS-KN.

b) *Pointing loss*: The small divergence of FSO beams requires a correspondingly accurate pointing of the transmitter terminal, as platform vibrations and other pointing inaccuracies result in a decrease of the received signal. The pointing loss, as a function of a stochastic angular jitter with standard deviation σ_{jitter} and systematic error θ_{bias} is given by [23]

$$\eta_{\text{pointing}} = \frac{\theta_{\text{div}}^2}{\theta_{\text{div}}^2 + 4\sigma_{\text{jitter}}^2} \exp\left(-\frac{2\theta_{\text{bias}}^2}{\theta_{\text{div}}^2 + 4\sigma_{\text{jitter}}^2}\right). \quad (14)$$

However, in a closed loop system there is a complex dependence of the jitter on the system parameters (including on the beam divergence itself) which is difficult to model. While a pointing jitter as small as $\sigma_{\text{jitter}} = 0.47 \mu\text{rad}$ has been demonstrated on a satellite downlink [24], which for a beam half-divergence $\theta_{\text{div}} = 5 \mu\text{rad}$ would correspond to a loss of only -0.15 dB , we prefer to use a more conservative estimate of $\sigma_{\text{jitter}} = 2.5 \mu\text{rad}$, resulting in a pointing loss $\text{dB}[\eta_{\text{pointing}}] = -3.0$.

c) *Atmospheric loss*: The propagation of an optical signal through the atmosphere results in losses due to absorption and scattering. The attenuation is described by a function $\alpha(h, \lambda)$ of the altitude h and of the wavelength λ and is typically expressed in dB/km. Then, the atmospheric loss can be computed as

$$\text{dB}[\eta_{\text{atm}}] = \frac{\int_{h_{\text{OGS}}}^{h_{\text{sat}}} \alpha(h, \lambda) dh}{\cos(\zeta)} \quad (15)$$

where ζ is the zenith angle of the satellite as seen at the OGS. Furthermore, $\alpha(h, \lambda)$ varies depending on location and weather conditions. We have fitted $\alpha(h, \lambda)$ from MODTRAN simulations [25], assuming a ground level visibility of 23 km, which represents an average working visibility condition. We have set $h_{\text{OGS}} = 602 \text{ m}$, the altitude above sea level of the OGS-KN.

d) *Receiver internal loss*: The receiver internal loss describes the attenuation within the receiver terminal, e.g., due to power attenuation on the optical surfaces. This loss depends on the total number of surfaces on the path of the optical signal and on their quality. Here we assume 7 mirrors with 95% reflectivity each, giving a total loss of around -1.5 dB .

e) *Transmitter internal loss*: For single-photon sources, transmitter internal losses must be taken into account as they directly impact the number of transmitted photons. However, in the case of Decoy-State BB84 with attenuated laser sources such losses can often be neglected. This is because the transmitted signal is already strongly attenuated to reach the few-quanta regime and set the pulse intensity used in the Decoy-State method. Therefore, if the value of the transmitter internal loss is known, it can be precompensated by including it in the total signal attenuation.

f) *Detector efficiency*: A critical aspect is the final coupling of the signal to the detector, which presents a non-trivial trade-off between two solutions: the use of fiber-coupled detectors or free-space-coupled ones. The analysis of the coupling efficiency from free-space to fiber is rather complex and depending on an accurate model of the employed Adaptive Optics (AO) system. For ease of analysis, in this work we have modeled the detector a free-space InGaAs Single-Photon Avalanche Detector (SPAD). This is a technology suitable for operation in the C-band, having an efficiency of 20%, approximately equal to -7 dB of loss, and a hold-off time after each detection of 100 ns.

IV. MODEL OF ATMOSPHERIC SCINTILLATION

The propagation of an optical signal through atmospheric turbulence results in intensity scintillation of the beam. The

origin of scintillation are wave-front distortions, resulting in self-interference of the beam after a certain propagation distance. A parameter that is used to evaluate the power fluctuations observed by the receiver due to scintillation is the Power Scintillation Index (PSI)

$$\sigma_{\text{scint}}^2 = \langle \eta_{\text{scint}}^2(t) \rangle - 1 \quad (16)$$

where we assume the normalization $\langle \eta_{\text{scint}}(t) \rangle = 1$. The fluctuation in the received optical power (proportional to η_{scint}) is averaged over a time that is longer than time scale over which the scintillation varies, given by the inverse of the Greenwood's frequency.

A. Modified Hufnagel-Valley Turbulence Model

Turbulence causes small-scale fluctuations in the index of refraction in Earth's atmosphere with a spatial correlation that, according to Kolmogorov's theory, approximately follows a power law. These fluctuations are primarily due to random variations in temperature and pressure, which lead to inhomogeneities in air density and, ultimately, to refractive index variations. As an optical beam propagates through these turbulent layers, these refractive index variations distort the phase front and redistribute the beam intensity, resulting in intensity scintillation.

The turbulence strength is quantified by the so-called index of refraction structure constant, C_n^2 . Its dependence on the altitude above seal level, h , is modeled starting from Hufnagel-Valley (HV) atmospheric turbulence profile [26], [27], which is the de-facto standard profile for modeling of atmospheric turbulence [28]. We employ a modified HV model, following the work in [29], which includes a correction factor F for the strength of turbulence in the boundary layer when the terrain is at a certain altitude h_{OGS} above sea level. This is given by

$$C_n^2(h) = 0.00594 \left(\frac{w}{27} \right)^2 (h \cdot 10^{-5})^{10} e^{-h/1000} + 2.7 \times 10^{-16} e^{-h/1500} + AF^2 e^{-\frac{(h-h_{\text{OGS}})}{100}} \quad (17)$$

where $w = 21 \text{ m/s}$ is the effective wind speed, $A = 1.7 \times 10^{-14} \text{ m}^{-2/3}$ is the turbulence at ground level. The correction factor is $F = 0.93$ for $h_{\text{OGS}} = 602 \text{ m}$.

B. Power Scintillation Index Calculation

The calculation of the PSI requires several intermediate steps. First, we start from computing Rytov parameter σ_{Ry}^2 , which corresponds to the (normalized) variance of the received power for point-like receivers, i.e. considering the optical intensity fluctuation on the axis of the beam, in the so-called weak turbulence condition. According to Rytov's first order perturbation theory, for a downlink beam (for which the plane wave approximation also holds) this quantity is given by

$$\sigma_{\text{Ry}} = \frac{2.25 k^{7/6}}{\cos^{11/6} \zeta} \int_{h_{\text{OGS}}}^{h_{\text{sat}}} C_n^2(h) (h - h_{\text{OGS}})^{5/6} dh \quad (18)$$

where $k = 2\pi/\lambda$ is the optical wave number and ζ is the zenith angle of observation.

Second, we need to take into account aperture averaging, using the approach presented in [30]. A beneficial effect in

FSO is that an extended receiver observes significantly reduced scintillation compared to a point-like receiver, especially when the beam spatial coherence length is much smaller than telescope aperture. This stems from the fact that adjacent regions of high and low power intensity within the telescope aperture will partially average each other out. First, we need to compute an effective link length, related to the length of the section of the link which is significantly affected by turbulence

$$L_{\text{eff}} = \frac{1}{\cos \zeta} \left(\frac{18 \int C_n^2(h) h^2 dh}{11 \int C_n^2(h) h^{5/6} dh} \right)^{6/7} \quad (19)$$

from which we can derive the aperture averaging scaling factor

$$f_{\text{aa}} = \left(1 + 1.062 d_{\text{aa}}^2 \right)^{-7/6}, \quad d_{\text{aa}} = D_{\text{OOG}} \sqrt{\frac{k}{4L_{\text{eff}}}} \quad (20)$$

so that the PSI for an extended receiver is $\sigma_{\text{scint}}^2 = f_{\text{aa}} \sigma_{\text{Ry}}^2$. However, this is valid only in the weak turbulence regime, which is not applicable when the satellite is at a low elevation angle. In order to derive an expression that applies to both the weak and strong turbulence conditions, we employ the following expression for the PSI, stemming from the use of the so-called extended Rytov theory [31, Chapter 10.3.2]:

$$\sigma_{\text{scint}}^2 = \exp \left[\frac{0.49 \sigma_{\text{Ry}}^2}{(1 + 0.65 d_{\text{aa}}^2 + 1.11 \sigma_{\text{Ry}}^{12/10})^{7/6}} + \frac{0.51 \sigma_{\text{Ry}}^2 (1 + 0.69 \sigma_{\text{Ry}}^{12/10})^{-5/6}}{1 + 0.9 d_{\text{aa}}^2 + 0.62 d_{\text{aa}}^2 \sigma_{\text{Ry}}^{12/10}} \right] - 1 \quad (21)$$

C. Greenwood's Frequency

The inverse of Greenwood's frequency defines the time scale over which the atmospheric turbulence varies. It is determined by the velocity with which turbulence cells move in front of the field of view of the telescope. This depends both on the wind speed and on the satellite motion. In this work we consider low wind speed conditions, so that we only need to consider the dominant contribution arising from the slew rate of the line-of-sight, for which we now derive an approximate expression.

From the orbit propagation software one can get the component of the satellite velocity orthogonal to the line-of-sight v_{sat}^{\perp} . From this a virtual wind speed associated to the slew rate of the line-of-sight can be computed as

$$V(h) = \frac{h - h_{\text{OOG}}}{h_{\text{sat}} - h_{\text{OOG}}} v_{\text{sat}}^{\perp}. \quad (22)$$

From the pseudo-wind $V(h)$ and the turbulence profile $C_n^2(h)$ one can compute Greenwood's frequency

$$f_{\text{G}} = 2.31 \lambda^{-6/5} \left(\frac{1}{\cos \zeta} \int C_n^2(h) V(h)^{5/3} dh \right)^{3/5}. \quad (23)$$

D. Scintillation Signal

The Probability Density Function (PDF) of the scintillation signal η_{scint} in a FSO downlink is accurately modeled by a lognormal distribution [31] and, furthermore, the Power Density Spectrum (PDS) is well approximated by a fourth

order Butterworth low-pass filter [32], [33]. We thus model the PDS of the scintillation signal in the Laplace domain as

$$H_{(t)}(s) = \left(1 + \left(\frac{s}{2\pi f_{\text{G}}(t)} \right)^{2n} \right)^{-1/2} \quad (24)$$

where $n = 4$ is the order of the filter and the cut-off frequency is given by Greenwood's frequency $f_{\text{G}}(t)$ which slowly varies in time during the satellite pass. The PDF of the scintillation signal is lognormal, given by

$$p_{(t)}(\eta_{\text{scint}}) = \frac{1}{\eta_{\text{scint}} \sqrt{2\pi \Sigma^2(t)}} \exp \left(-\frac{[\ln(\eta_{\text{scint}}) + \frac{1}{2}\Sigma^2(t)]^2}{2\Sigma^2(t)} \right) \quad (25)$$

with $\Sigma^2(t) = \ln(\sigma_{\text{scint}}^2(t) + 1)$. This PDF has mean 1 and has variance $\sigma_{\text{scint}}^2(t)$ which slowly changes in time.

V. MODEL OF THE QKD SIGNAL

Here we model the signal observed by the receiver in a Decoy-State BB84 protocol with active basis choice [34]. The receiver consists of a polarization rotation stage, which may apply a 45° rotation to the incoming photons, followed by a polarizing beam splitter that directs the signal to two single-photon detectors. The detectors are modeled as ideal threshold devices, registering a click whenever one or more photons arrive. We label them as correct (✓) and incorrect (✗), depending on whether the outcome matches Alice's transmitted polarization.

When Alice transmits pulses at a rate $R_{\text{Tx}} = 1 \text{ GHz}$ with mean photon number α (signal $\alpha = \mu$, decoy $\alpha = \nu$, or vacuum $\alpha = 0$), the expected number of received photons is $\eta(t)\alpha$, where η includes channel transmittance and detector efficiency. The total expected photon numbers at the detectors are

$$\begin{cases} \tau_{\checkmark, \alpha} = \eta(t) \cdot \alpha \cos^2(\delta_{\text{mis}}) + r_{\text{noise}}, \\ \tau_{\times, \alpha} = \eta(t) \cdot \alpha \sin^2(\delta_{\text{mis}}) + r_{\text{noise}}, \end{cases} \quad (26)$$

where $\delta_{\text{mis}} = 5^\circ$ is the misalignment between the transmitter and receiver reference frames, and r_{noise} accounts for background light and detector dark counts. The noise term is expressed as the number of effective noise photons per detection window of duration $1/R_{\text{Tx}}$, i.e., $r_{\text{noise}} = R_{\text{noise}}/R_{\text{Tx}} = 3 \cdot 10^{-6}$ for a noise photon rate $R_{\text{noise}} = 3 \text{ kHz}$.

Since photon arrivals follow a Poisson distribution, the click probabilities for the two detectors are

$$p(\checkmark | \alpha) = 1 - e^{-\tau_{\checkmark, \alpha}}, \quad p(\times | \alpha) = 1 - e^{-\tau_{\times, \alpha}}. \quad (27)$$

If both detectors click, the outcome is randomly assigned to one of them.

The resulting QBER is the ratio of erroneous to total detection events (including both single-clicks and double-clicks):

$$Q(\alpha) = \frac{p(\text{err} | \alpha)}{p(\text{click} | \alpha)} = \frac{p(\times | \alpha) - \frac{1}{2} p(\checkmark | \alpha) p(\times | \alpha)}{p(\checkmark | \alpha) + p(\times | \alpha) - p(\checkmark | \alpha) p(\times | \alpha)}. \quad (28)$$

This expression applies to both the Z and X bases. Note that $Q(\alpha)$ decreases monotonically with α and satisfies $Q(0) = \frac{1}{2}$.

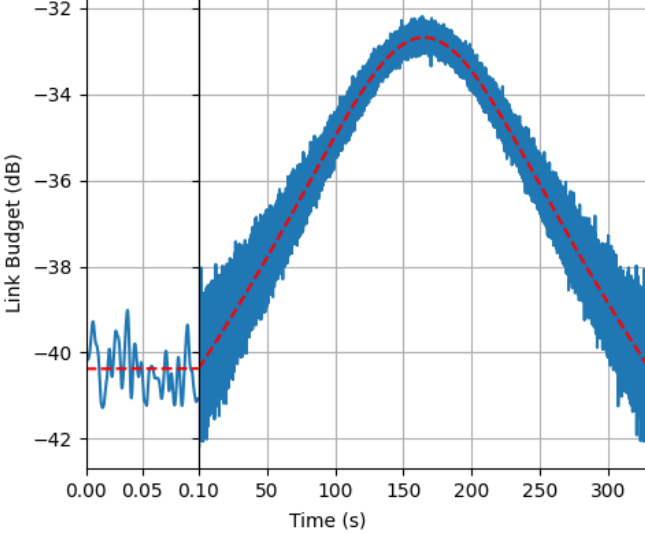


Fig. 1: Simulated downlink end-to-end efficiency (i.e., link budget) for the reference satellite pass, including (solid, blue) and excluding (dashed, red) scintillation effects. Left: zoom-in of the first 100 ms of the pass.

VI. SIMULATION METHODOLOGY

The satellite orbit was selected from the KIODO measurement campaign conducted by DLR [21]. The simulated pass has a total duration of $T_{\text{pass}} = 330$ s. For each second, the corresponding elevation angle and link distance are provided by the orbit propagation software.

The simulation is structured in three main parts: (i) generation of a scintillation time series, (ii) simulation of QKD signal transmission over the resulting channel, and (iii) execution of an IR protocol on the simulated data.

A. Generation of the Scintillation Time Series

In order to generate a simulated scintillation signal with a specified PDF and PDS, we employ the approach introduced in [35]. The procedure starts by drawing normalized Gaussian random variables $\mathbf{u} = \{u(t_i)\}_i$ where the times t_i are sampled at a sufficiently high frequency, here chosen as $R_{\text{sample}} = 40$ kHz. A linear filter \mathbf{h} is then applied to the vector \mathbf{u} to introduce the time correlations specified by the PDS, giving $\mathbf{v} = \mathbf{h} * \mathbf{u}$. This is followed by a zero-memory (i.e., point-wise) nonlinear transformation to match the target PDF.

The slowly-varying Butterworth filter in (24) is applied to the array \mathbf{u} of Gaussian random variables. Typically, the filter is applied in the Fourier domain, where convolution reduces to point-wise multiplication and is thus computationally efficient. However, due to the explicit time dependence of the filter, we instead perform the operation in the time domain by convolving with $h_{(t)}(\tau) = \mathcal{L}^{-1}\{H_{(t)}\}(\tau)$, the inverse Laplace transform of (24). For computational efficiency, we introduce a parameter $\tau_{\text{corr}}^{\max}$ beyond which correlations among scintillation values are considered negligible, and approximate $h_{(t)}(\tau) \simeq 0$ for $\tau > \tau_{\text{corr}}^{\max}$. Here we set $\tau_{\text{corr}}^{\max} = 0.03$ s, such that $h_{(t)}(\tau)$ is

evaluated at $n_{\max} = R_{\text{sample}}\tau_{\text{corr}}^{\max} = 1200$ points. We then define the function

$$\tilde{h}_{(t)}(\tau) = \begin{cases} h_{(t)}(\tau) & \text{if } \tau \leq \tau_{\text{corr}}^{\max}, \\ 0 & \text{otherwise,} \end{cases} \quad (29)$$

where $t_{\Delta} = \lfloor t/\Delta + 0.5 \rfloor \Delta$, meaning that $\tilde{h}_{(t)}$ is updated once per time interval Δ . In this work we set $\Delta = 1$ s. The filtering operation is then expressed as the discrete convolution

$$v(t_i) = (\tilde{h}_{(t)} * u)(t_i) = \sum_{j=0}^{n_{\max}} \tilde{h}_{(t)}(t_j) u(t_i - t_j). \quad (30)$$

The overall time complexity of the algorithm is $O(n_{\max}N_{\text{tot}})$, where the total number of points is $N_{\text{tot}} = T_{\text{pass}}R_{\text{sample}} = 13.2 \cdot 10^6$.

Next, the zero-memory nonlinear transformation $\mathcal{F}_{(t)}(V) = \exp(V\Sigma(t) - \Sigma^2(t)/2)$ is applied, mapping Gaussian variables to the lognormal distribution $p_{(t)}$ defined in (25). The resulting scintillation signal is $\eta_{\text{scint}}(t) = \mathcal{F}_{(t)}(v(t))$.

Finally, the scintillation signal is combined with the rest of the link budget to obtain the end-to-end efficiency $\eta(t)$ over the entire satellite pass. The result is shown in Fig. 1.

B. Generation of Simulated QKD Signals

The global transmission $\eta(t)$ is then used to simulate a Decoy-State BB84 protocol. The outputs consist of an array indicating the click times at Bob's receiver and, for those corresponding to Z-basis measurements (the basis used for key generation), Alice's sifted key \mathbf{z}_A and the error vector \mathbf{e} , where Bob's sifted key is $\mathbf{z}_B = \mathbf{z}_A \oplus \mathbf{e}$. In addition, an array containing the QBER associated with each click is generated. This information is crucial for enhancing the performance of the IR procedure.

We first generate the click instants $\mathbf{c} = \{c_i\}_{i=1}^{n_{\text{click}}}$. The possible click instants are expressed as integers between 0 and $T_{\text{pass}}R_{\text{Tx}} - 1$, where $T_{\text{pass}}R_{\text{Tx}} = 330 \cdot 10^9$ is the total number of transmitted pulses. Since the probability of a click is very low (always less than 10^{-3} in our scenario), one could, in principle, use a geometric random variable $G \sim \text{Geo}(p_{\text{click}})$ to directly sample the next click instant, where p_{click} is obtained by averaging $p(\text{click}|\alpha)$ over α .

However, two aspects must be taken into account: (i) the detector remains inactive for a time $t_{\text{hold-off}}$ after each click, and (ii) p_{click} depends on $\eta(t)$ and thus varies with time. Since the downlink transmission $\eta(t)$ is sampled at a rate R_{sample} , p_{click} only changes with this frequency. The number of transmission instants for which the conditions remain constant is therefore

$$n_{\text{window}} = \frac{R_{\text{Tx}}}{R_{\text{sample}}}. \quad (31)$$

Let c_i denote the current click instant. The next click instant c_{i+1} is sampled as follows. We initialize an auxiliary variable $\theta \leftarrow c_i + n_{\text{hold-off}}$, where $n_{\text{hold-off}} = t_{\text{hold-off}} \cdot R_{\text{Tx}}$ is the number of instants during which the detector is inactive after a click. We then draw $G \sim \text{Geo}(p_{\text{click}}(\theta))$ and set a tentative time increment $\theta' \leftarrow \theta + G$. If (case a) the condition $\lfloor \theta'/n_{\text{window}} \rfloor = \lfloor \theta/n_{\text{window}} \rfloor$ holds, then θ' lies within an

interval in which p_{click} is constant, and we set $c_{i+1} = \theta'$. Otherwise (case *b*) θ' exceeds the interval, making the draw invalid. In this case, by exploiting the memoryless property of the process, we advance θ to the start of the next window, i.e., $\theta \leftarrow n_{\text{window}}(\lfloor \theta/n_{\text{window}} \rfloor + 1)$, and repeat the procedure until case *a* is satisfied. This process continues until the end of the satellite pass, yielding the vector of click instants \mathbf{c} .

Each click is then assigned, a posteriori, the bases in which Alice prepared the photon and Bob performed the measurement, with probabilities p_Z and $p_X = 1 - p_Z$, so that the joint probability of both using the Z basis is p_Z^2 . For each Z event, a uniformly random value is drawn to generate Alice's sifted key \mathbf{z}_A . Next, an intensity α is assigned to each click event according to $p(\alpha|\text{click})$, obtained via Bayes' rule from the known values $p(\text{click}|\alpha)$ and p_α . A vector of QBER values $\mathbf{q} = \{q_i\}_i$ is then computed for each sifted Z bit using Eq. (28). Finally, the error vector \mathbf{e} is constructed by setting each bit e_i to 1 with probability q_i and to 0 otherwise.

C. Simulation of IR

Finally, IR is performed on the simulated data using a Dynamic-Link Library (DLL) that implements the rateless protograph LDPC codes described in [13], kindly provided by the authors. The inputs to the library are: Φ , a scalar QBER parameter used to select the initial code family; \mathbf{z}_A and \mathbf{z}_B , the sifted keys of Alice and Bob; and an array of instantaneous LLR values \mathbf{llr} . The LLR values convey the reliability of each bit to the decoder and are computed as

$$\text{llr}_i = \ln\left(\frac{1 - q_i}{q_i}\right). \quad (32)$$

The results of the IR simulations, obtained under different strategies to identify the most effective configurations, are presented in Sec. VII.

VII. SIMULATION RESULTS

The QBER array obtained from the QKD simulation contains more than 35 million values. For IR, the sequence is divided into blocks of length $N_{\text{bl}} = 460800$, which is a multiple of 1800, as required by the codes in [13]. The last remaining k bits are assigned to a block of length equal to the largest multiple of 1800 not exceeding k , to minimize discarded bits. Moreover, as shown in Fig. 1, the signal tails correspond to the lowest transmittance and thus the highest QBER values, leading to poorer reconciliation rates.

The first comparison addresses the choice of Φ for code selection: either the mean QBER in the block or the QBER corresponding to the mean channel capacity of the block. In [13], this distinction is not considered because a constant QBER is assumed, and the two coincide. Although the former is a simpler approximation, the latter provides a code rate matched to the effective information transmitted through the noisy channels.

With the mean QBER approach,

$$\Phi_j = \frac{1}{N_{\text{bl}}} \sum_{i=N_j}^{N_j+N_{\text{bl}}-1} q_i, \quad (33)$$

where N_j is the starting index of the j -th block. Alternatively, each bit is modeled as being transmitted through its own Binary Symmetric Channel (BSC) with error probability q_i . The mean capacity of the sequence of BSCs is then

$$C_j = 1 - \frac{1}{N_{\text{bl}}} \sum_{i=N_j}^{N_j+N_{\text{bl}}-1} h_2(q_i), \quad (34)$$

and the equivalent QBER Φ_j is obtained by solving $C_j = 1 - h_2(\Phi_j)$ by bisection.

As shown in Fig. 2a, the red curve (mean channel capacity) is consistently above the blue curve (mean QBER), except for block 56, likely due to statistical fluctuations. The average rate is also higher. Therefore, all subsequent simulations adopt Φ computed via the mean channel capacity.

A second study evaluates the impact of different strategies for passing the optional variable \mathbf{llr} :

- 1) Excluding \mathbf{llr} entirely.
- 2) Using block-wise average QBER values for each intensity (signal, decoy, vacuum). In other words, if a particular instant clicked when the state was the decoy, the \mathbf{llr} array in that particular instant will have as a value the average QBER of decoy states for the entire block (and analogously for the signal and vacuum states).
- 3) Using the full LLR array from the QKD simulation.

Figure 2b shows that strategies 2 and 3 yield identical rates for each block and significantly outperform strategy 1. This demonstrates that comparable performance can be achieved either by retaining full LLR information or, more efficiently, by tracking only block-wise averages of the signal, decoy, and vacuum states.

For subsequent comparisons, the curve with full LLR information (red in Fig. 2b) is taken as the baseline.

A further strategy was to randomize the order of detection events, with the rationale that high-quality signals (central part of the curve) could assist in correcting lower-quality ones (tails). However, Fig. 2c shows that the randomized rates, now constant across blocks, are slightly lower than the average baseline.

Another approach was to corrupt the \mathbf{llr} values by adding Gaussian noise with mean 0 and standard deviation 0.125. As shown in Fig. 2d, this significantly reduces the rates, highlighting the importance of accurate LLR estimation.

Next, the DLL was provided with a modified LLR vector \mathbf{llr}' , identical to \mathbf{llr} but excluding vacuum events. Since vacuum states yield $\text{QBER} \simeq 0.5$, they may require more bits to correct than their contribution to the sifted key. Figure 2e shows that this strategy improves the reconciliation rate compared to the baseline, but since the sifted key length is reduced (by about 90 000 vacuum events), the overall SKL improvement is marginal. Indeed, as confirmed in Fig. 3, this approach yields only a slight increase.

Finally, the same vacuum exclusion strategy was combined with block-wise averages for signal and decoy states. As shown in Fig. 2f, this performs almost identically to the full \mathbf{llr} vector without vacuum events. The latter produces only 60 additional secret key bits over nearly seven million, confirming the negligible difference.

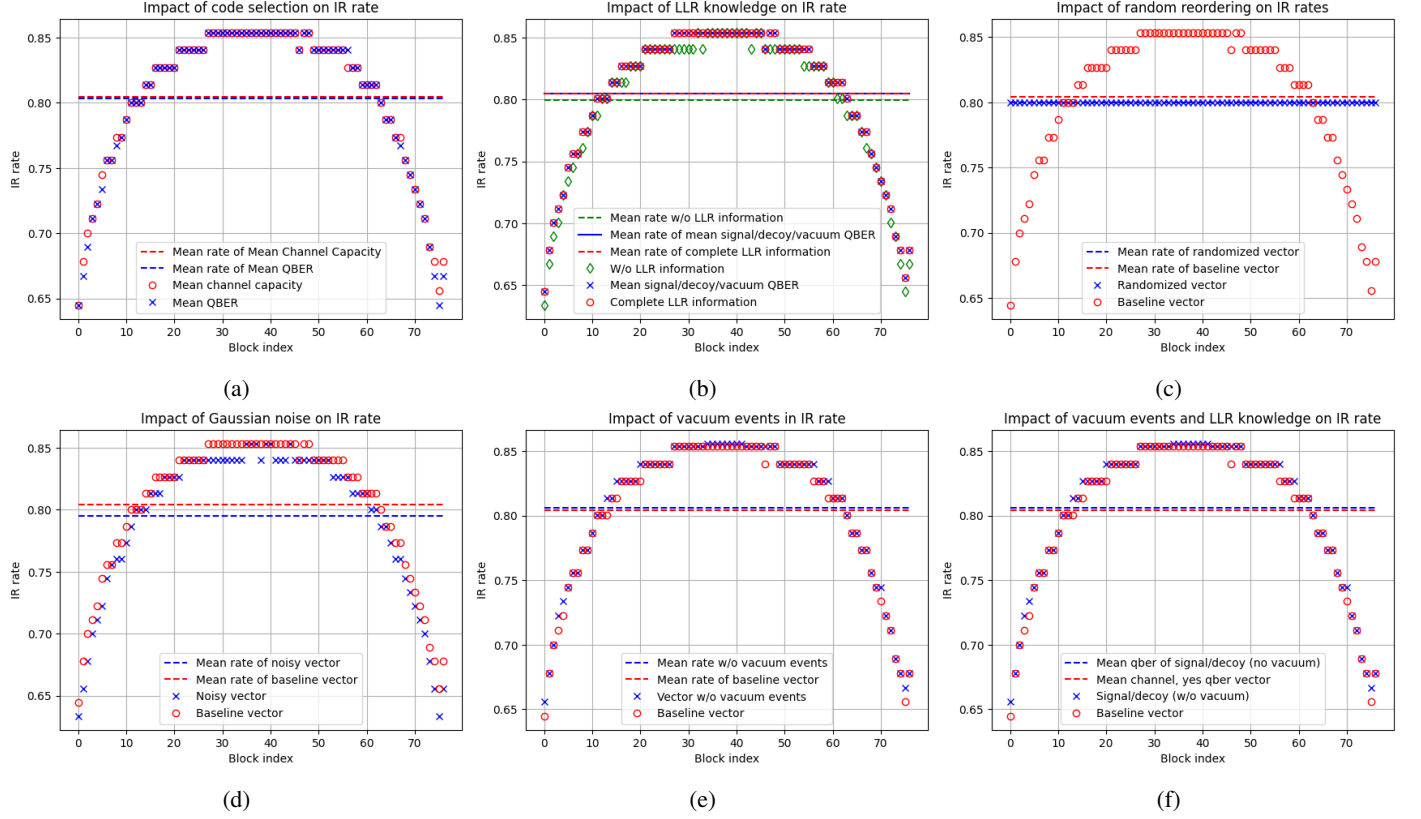


Fig. 2: On the x -axis are the indexes of the blocks used in IR, and on the y -axis are the corresponding IR rates, obtained via Eq. (3) from the DLL output. (a) Mean channel capacity vs. mean QBER for code selection; in the following figures the mean channel capacity is always used for code selection. (b) Complete LLR knowledge vs. mean signal/decoy/vacuum vs. mean block-wise QBER; in the following figures complete LLR knowledge is used as baseline. (c) Baseline vs. bit position randomization strategy. (d) Baseline vs. noisy LLR information. (e) Baseline vs. complete LLR without vacuum states. (f) Baseline vs. mean signal/decoy without vacuum states.

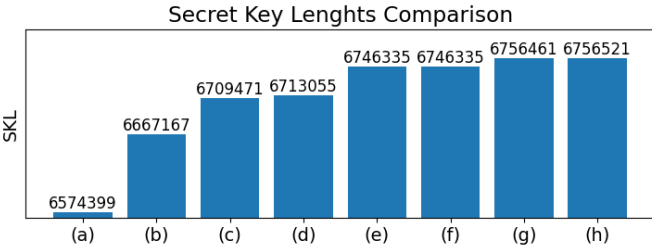


Fig. 3: Comparison of the SKL obtained under the following strategies: a) no **llr**; b) baseline (case (e)) with bit position randomization; c) noisy LLR estimation; d) LLR vector with mean QBER for code selection; e) LLR vector with mean channel capacity for code selection (baseline); f) three LLR values for signal/decoy/vacuum; g) two LLR values for signal/decoy, excluding vacuum events; h) baseline (case (e)), excluding vacuum events.

VIII. CONCLUSIONS

In this work, we improved the performance of information reconciliation (IR) for Decoy-State BB84 in a simulated satellite downlink scenario. To achieve this, we employed a comprehensive channel model that accounts for the time-

varying link budget and a realistic quantum receiver model, allowing us to accurately simulate the instantaneous QBER throughout a satellite pass. These values were then used to generate log-likelihood ratio information for the decoder, thereby improving efficiency, reducing information leakage to the eavesdropper, and ultimately yielding a longer secure key from the same quantum communication data.

Our primary finding is that leveraging a-priori knowledge of the instantaneous QBER to inform the low-density parity check (LDPC) decoder enhances the efficiency of IR, increasing the secret key length (SKL) by nearly 3% compared to the standard approach that assumes a uniform error rate across the block. Several reconciliation strategies were evaluated to identify the most effective scheme. We found that initializing rateless code selection based on the mean channel capacity of each block consistently outperforms using the mean QBER. Performance was observed to be highly sensitive to the accuracy of QBER estimation. Notably, a simpler strategy that assigns block-wise average QBER values for signal, decoy, and vacuum states performed nearly identically to the full instantaneous-information case, offering a practical trade-off between complexity and performance. The highest SKL, albeit by a narrow margin, was obtained by excluding detections

from vacuum states; despite producing a smaller sifted key, this approach yielded a slightly longer final secret key. By contrast, strategies such as bit-order randomization degraded performance. A summary of these results is shown in Fig. 3.

Overall, the LDPC-based IR scheme demonstrated very high performance compared with alternatives in the literature, with the inefficiency factor ranging from $f = 1.11166$ for the best-performing strategy to $f = 1.1386$ for the worst case, where no instantaneous QBER information was provided.

Future research may explore alternative bit-ordering methods to further optimize decoder performance. Additionally, investigating the real-time implementation of these schemes in hardware would be a valuable step toward practical deployment of more efficient satellite QKD systems.

ACKNOWLEDGMENTS

We thank Dr. Alberto Tarable for adapting the software implementing message passing decoding for protograph LDPC codes. This work was done within the project QuNET funded by the German Federal Ministry of Education and Research under the funding code 16KIS1265.

REFERENCES

- [1] P. W. Shor, "Algorithms for quantum computation: discrete logarithms and factoring," in *Proc. 35th Annu. Symp. on Foundations of Computer Science*. Ieee, 1994, pp. 124–134.
- [2] J. Proos and C. Zalka, "Shor's discrete logarithm quantum algorithm for elliptic curves," *arXiv preprint quant-ph/0301141*, 2003.
- [3] (2025) First qkd cryptographic system certified - win-lab. [Online]. Available: <https://www.win-labor.dfn.de/en/2025/02/17/first-qkd-cryptographic-system-certified/>
- [4] D. Orsucci, P. Kleinpaß, J. Meister, I. De Marco, S. Häusler, T. Strang, N. Walenta, and F. Moll, "Assessment of practical satellite quantum key distribution architectures for current and near-future missions," *International Journal of Satellite Communications and Networking*, vol. 43, no. 3, pp. 164–192, 2025.
- [5] S.-K. Liao, W.-Q. Cai, W.-Y. Liu, L. Zhang, Y. Li, J.-G. Ren, J. Yin, Q. Shen, Y. Cao, Z.-P. Li *et al.*, "Satellite-to-ground quantum key distribution," *Nature*, vol. 549, no. 7670, pp. 43–47, 2017.
- [6] S.-K. Liao, W.-Q. Cai, J. Handsteiner, B. Liu, J. Yin, L. Zhang, D. Rauch, M. Fink, J.-G. Ren, W.-Y. Liu *et al.*, "Satellite-relayed intercontinental quantum network," *Phys. Rev. Lett.*, vol. 120, no. 3, p. 030501, 2018.
- [7] Y. Li, W.-Q. Cai, J.-G. Ren, C.-Z. Wang, M. Yang, L. Zhang, H.-Y. Wu, L. Chang, J.-C. Wu, B. Jin *et al.*, "Microsatellite-based real-time quantum key distribution," *Nature*, pp. 1–8, 2025.
- [8] J. P. Armengol, G. Acar, N. Lindman, Z. Sodnik, R. M. Calvo, C. A. Vasko, K. Balakier, and H. Hauschildt, "Optical technologies for connectivity and secure communications," in *IEEE Int. Conf. on Space Optical Systems and Applications (ICOSOS)*. IEEE, 2023, pp. 8–15.
- [9] T. Hiemstra, D. Hasler, D. Paone, F. Reichert, F. Heine, and J. Struck, "The european satellite-based QKD system EAGLE-1," in *Free-Space Laser Commun. XXXVII*, vol. 13355. SPIE, 2025, pp. 216–222.
- [10] B. Rödiger, R. Rüddenkau, L. Elsner, T. Petermann, and P. Bangert, "First in-orbit results of the QUBE mission hosting a laser communication terminal for experiments towards quantum key distribution from CubeSats," in *SmallSat Europe 2025*, May 2025. [Online]. Available: <https://elib.dlr.de/214414/>
- [11] M. Hutterer, M. Auer, A. Baluika, O. Bayraktar, P. Freiwang, M. Gall, K. Günther, R. Haber, J. Janusch, L. Knips, P. Kobel, M. Krauss, N. Lemke, C. Marquardt, F. Moll, C. Papadopoulos, J. Pudelko, B. Rödiger, C. Roubal, J. Scharnagel, K. Schilling, C. Schmidt, and H. Weinfurter, "QUBE-II - quantum key distribution with a CubeSat," in *73rd Int. Astronautical Congress, IAC 2022*, September 2022. [Online]. Available: <https://elib.dlr.de/190981/>
- [12] J. Martinez-Mateo, C. Pacher, M. Peev, A. Ciurana, and V. Martin, "Demystifying the information reconciliation protocol cascade," *arXiv preprint arXiv:1407.3257*, 2014.
- [13] A. Tarable, R. P. Paganelli, and M. Ferrari, "Rateless protograph LDPC codes for quantum key distribution," *IEEE Trans. Quantum Eng.*, vol. 5, pp. 1–11, 2024.
- [14] J. Thorpe, "Low-density parity-check (LDPC) codes constructed from protographs," *IPN progress report*, vol. 42, no. 154, pp. 42–154, 2003.
- [15] C. H. Bennett and G. Brassard, "Quantum cryptography: Public key distribution and coin tossing," *Theoretical computer science*, vol. 560, pp. 7–11, 2014.
- [16] S. Pirandola, U. L. Andersen, L. Banchi, M. Berta, D. Bunandar, R. Colbeck, D. Englund, T. Gehring, C. Lupo, C. Ottaviani *et al.*, "Advances in quantum cryptography," *Advances in optics and photonics*, vol. 12, no. 4, pp. 1012–1236, 2020.
- [17] H.-K. Lo, X. Ma, and K. Chen, "Decoy state quantum key distribution," *Phys. Rev. Lett.*, vol. 94, no. 23, p. 230504, 2005.
- [18] C. C. W. Lim, M. Curty, N. Walenta, F. Xu, and H. Zbinden, "Concise security bounds for practical decoy-state quantum key distribution," *Phys. Rev. A*, vol. 89, no. 2, p. 022307, 2014.
- [19] J. Wiesemann, J. Krause, D. Tupkary, N. Lütkenhaus, D. Rusca, and N. Walenta, "A consolidated and accessible security proof for finite-size decoy-state quantum key distribution," *arXiv preprint arXiv:2405.16578*, 2024.
- [20] I. Devetak and A. Winter, "Distillation of secret key and entanglement from quantum states," *Proc. of the Royal Society A: Mathematical, Physical and Eng. Sciences*, vol. 461, no. 2053, pp. 207–235, 2005.
- [21] D. Giggenbach, F. Moll, and N. Perlot, "Optical communication experiments at DLR," *J. of the National Institute of Information and Commun. Technol.*, vol. 59, no. 1.2, pp. 125–134, 2012.
- [22] H. T. Friis, "A note on a simple transmission formula," *Proc. of the IRE*, vol. 34, no. 5, pp. 254–256, 1946.
- [23] A. Carrillo-Flores, D. Giggenbach, M. Knopp, D. Orsucci, and A. Shrestha, "Effects of pointing errors on intensity losses in the optical LEO uplink," in *Int. Conf. on Space Optics—ICSO 2022*, vol. 12777. SPIE, 2023, pp. 2476–2491.
- [24] X. Wang, C. Li, J. Jia, J. Wu, R. Shu, L. Zhang, and J. Wang, "Angular micro-vibration of the Micius satellite measured by an optical sensor and the method for its suppression," *Applied optics*, vol. 60, no. 7, pp. 1881–1887, 2021.
- [25] A. Berk, P. Conforti, R. Kennett, T. Perkins, F. Hawes, and J. Van Den Bosch, "Modtran® 6: A major upgrade of the modtran® radiative transfer code," in *2014 6th Workshop on Hyperspectral Image and Signal Processing: Evolution in Remote Sensing (WHISPERS)*. IEEE, 2014, pp. 1–4.
- [26] R. E. Hufnagel, "Propagation through atmospheric turbulence," *The Infrared Handbook*, vol. 6, pp. 1–56, 1978.
- [27] G. C. Valley, "Isoplanatic degradation of tilt correction and short-term imaging systems," *Applied Optics*, vol. 19, no. 4, pp. 574–577, 1980.
- [28] L. C. Andrews, *Field guide to atmospheric optics*, 2019.
- [29] R. M. Calvo, "Correction factor," 2025/2026, work in preparation.
- [30] H. T. Yura, "Optical downlink propagation from space-to-earth: aperture-averaged power fluctuations, temporal covariance and power spectrum," *Optics Express*, vol. 26, no. 21, pp. 26 787–26 809, 2018.
- [31] L. C. Andrews and M. K. Beason, *Laser beam propagation in random media: new and advanced topics*, 2023.
- [32] K.-H. Kim, T. Higashino, K. Tsukamoto, and S. Komaki, "Optical fading analysis considering spectrum of optical scintillation in terrestrial free-space optical channel," in *Int. Conf. on Space Optical Systems and Applications (ICSO)*, 2011, pp. 58–66.
- [33] G. La Torre, S. Raffa, J. Poliak, A. P. Reeves, and I. Hristovski, "A spectral shaping approach to generate power vectors for optical ground-to-space links," in *Environmental Effects on Light Propagation and Adaptive Systems VII*, vol. 13194. SPIE, 2024, pp. 145–160.
- [34] S. Häusler, D. Orsucci, L. Vollmann, E. Peev, and F. Moll, "Measurement-based characterization of atmospheric background light in satellite-to-ground quantum key distribution scenarios," *Optical Eng.*, vol. 63, no. 4, pp. 041211–041211, 2024.
- [35] U. Gujar and R. Kavanagh, "Generation of random signals with specified probability density functions and power density spectra," *IEEE Trans. Autom. Control*, vol. 13, no. 6, pp. 716–719, 1968.